ACS APPLIED MATERIALS & INTERFACES

Research Article

www.acsami.org

Decohesion Kinetics in Polymer Organic Solar Cells

Christopher Bruner, Fernando Novoa, Stephanie Dupont, and Reinhold Dauskardt*

Department of Materials Science and Engineering, Stanford University, 496 Lomita Mall, Durand Building, Stanford, California 94305-2205, United States

Supporting Information

ABSTRACT: We investigate the role of molecular weight (M_W) of the photoactive polymer poly(3-hexylthiophene) (P3HT) on the temperature-dependent decohesion kinetics of bulk heterojunction (BHJ) organic solar cells (OSCs). The M_W of P3HT has been directly correlated to its carrier field effect mobilities and the ambient temperature also affects OSC in-service performance and P3HT arrangement within the BHJ layer. Under inert conditions, time-dependent decohesion readily occurs within the BHJ layer at loads well below its fracture resistance. We observe that by increasing the M_W of P3HT, greater resistance to decohesion is achieved. However, failure consistently occurs within the BHJ layer representing the weakest layer within the device stack. Additionally, it was found that at temperatures below the glass transition temperature (~41−45 °C), decohesion was characterized by brittle failure via molecular bond rupture. Above the glass transition temperature, decohesion growth occurred by a viscoelastic process in the BHJ layer, leading to a significant degree of viscoelastic deformation. We develop a viscoelastic model based on molecular relaxation to describe the resulting behavior. The study has implications for OSC long-term reliability and device performance, which are important for OSC production and implementation.

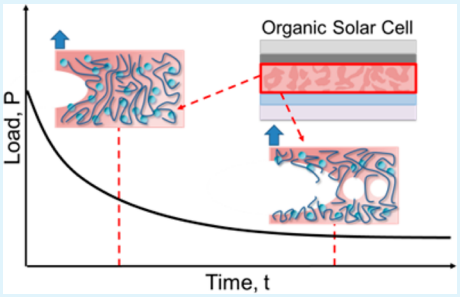

KEYWORDS: *fullerenes, solar cells, thin films, fracture, polymer*

INTRODUCTION

Inexpensive, flexible bulk heterojunction (BHJ) organic solar cells (OSCs) are one of many promising alternative energy technologies that may aid in addressing our growing need to build a sustainable future.[1−4] Indeed, large-scale solar parks have already begun utilizing state-of-the-art roll-to-roll produced OSCs in which placement and replacement of these solar sheets is fully automated.[5] However, challenges remain that limit their wider adoption and implementation. Among these are optimized power conversion efficiency (PCE), chemical stability, and mechanical reliability.[2,6−9] In this study, we investigate the time-dependent decohesion of standard polymer OSC architectures under controlled environmental conditions and varying temperatures. This will ultimately provide valuable insight into improving and optimizing OSC mechanical reliability.

In several recent studies, the cohesive/adhesive energy, G_C (J m^{-2}), of standard and roll-to-roll OSCs was measured.[7,8,10] It was shown that the polymer BHJ layer and adjacent interfaces in standard and inverted roll-to-roll OSCs fail with relatively low cohesive energy (G_C ~1−2 J m^{-2}). These studies also indicated that cohesive failure predominantly occurred for standard OSC architectures but inverted roll-to-roll OSCs would fail adhesively due to changes in interface energy. However, significant improvements could be made depending on the BHJ layer composition, polymer/fullerene ordering, and thermal annealing time and temperature to give G_C values of ~5 J m^{-2}. More recently, it was shown that by increasing the semiconducting polymer weight average molecular weight (M_W) and BHJ layer thickness, significant increases to the cohesive energy of the layer could be achieved (G_C up to 17 J m^{-2}) due to plasticity at the decohesion tip, which helped to dissipate mechanical energy.[11] Although G_C is a measure the cohesive fracture energy, many materials exhibit a time-dependent loss of cohesion at values of $G < G_C$. This time dependency is often associated with temperature and environmental effects that may weaken chemical bonds. Decohesion studies of the polymers poly(3,4-ethyl-enedioxythiophene) poly(styrene-sulfonate) (PEDOT:PSS) and OSC encapsulant ethylene-vinyl-acetate (EVA) have measured the decohesion rates (da/dt) as a function of G to show that the ambient temperature, relative humidity and aging time strongly influenced how quickly and how far decohesion would extend within the material.[12,13]

In this study, we used a single-cantilever beam (SCB) testing method to investigate the effects of temperature and the M_W of the semiconducting polymer, poly(3-hexylthiophene) (P3HT), on the decohesion kinetics of the BHJ layer (consisting of electron donating P3HT and electron accepting fullerene phenyl-C61-butyric acid methyl ester ($PC_{60}BM$)) (Figure 1).[13,14] This technique permits observation of decohesion rate by monitoring the load relaxation associated with decohesion within the OSC. Because SCB primarily acts in tension relative to the surface, we characterize time-dependent failure, which may be exacerbated by factors like thermal expansion mismatch of the layers. We show that at room

Received: September 21, 2014
Accepted: November 4, 2014
Published: November 4, 2014

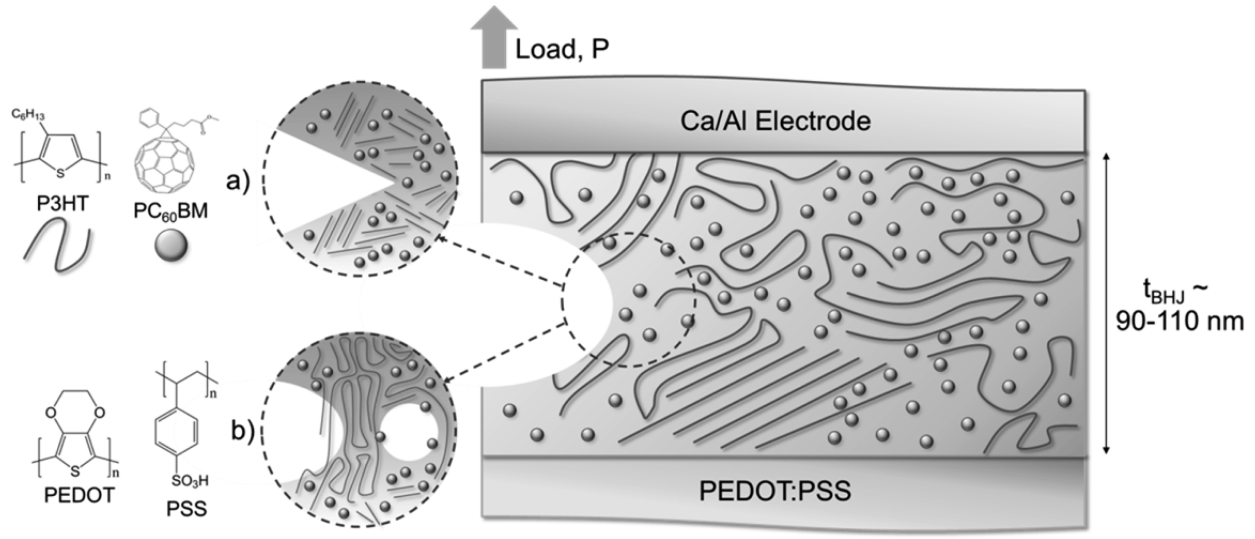

Figure 1. BHJ layer of OSC consisting of P3HT:$PC_{60}BM$. A close up of the crack tip for BHJs made from (a) low M_W P3HT and (b) high M_W P3HT. In the case of panel a, the crack may extend between the polymer regions with ease, but for panel b, large domains of entangled and bridged P3HT limit crack growth.

temperature, regardless of P3HT M_W, decohesion occurred very rapidly before arresting, similar to brittle solids. However, as the test temperature was raised above the glass transition temperature, T_g, of the BHJ layer, significant viscoelasticity characterizes the decohesion. With increasing temperatures, we see a reduction in the cohesive threshold, G_{th}, where growth rates fall below 10^{-9} m s^{-1}. Finally, we are able to model this viscoelastic crack growth behavior using a kinetic model we developed to understand the changing mechanical response to temperature. Understanding the decohesion kinetics in terms of modeling the molecular relaxations will provide greater insight into assessing and improving the in-service lifetimes of polymer OSCs and other organic electronics.

EXPERIMENTAL SECTION

Thermal Analysis. DSC and MTDSC methods were performed using a TA Instruments Q2000 differential scanning calorimeter with an RCS cooling system. Sapphire was used to calibrate the cell capacitance. Samples were harvested from drop-casted thin films of the BHJ layer from clean glass slides. Anywhere from 10 to 15 mg of samples were placed into Tzero aluminum hermetically sealed DSC pans and the T4P heat flow signal was monitored to account for pan effects. Nitrogen was used as a purge gas with flow rate of 50 mL min^{-1}. DSC scan rate was set to 10 °C min^{-1}. Test started at the lower limit of −60 °C, held for 10 min, then ramped to the upper limit of 310 °C and allowed to settle for 1 min. The sample was allowed to cool back down to −60 °C and held for 1 min. MTDSC was then employed to investigate the T_g of the samples. Modulation amplitude was set to 1 °C with period of 60 s. The samples were heated to 310 °C at 2.5 °C min^{-1} and held for 1 min before being finally cooled back to −60 °C.

OSC Preparation. OSCs were fabricated with using regioregular poly-(3-hexylthiophene-2,5-diyl) (P3HT) (Rieke Metals) of varying M_W. Batch data is provided in the Supporting Information (Table S1). All OSCs were fabricated on top of 30 ± 5 nm of PEDOT:PSS covered indium tin oxide (ITO, 120 nm) glass substrates (50 × 50 ×0.7 mm). The BHJ layer, consisting of P3HT and phenyl-C61-butyric acid methyl ester ($PC_{60}BM$, Solenne, Purity >99.5%) in a 1:1 mass ratio, was spun cast from solutions with total solute concentration of 25 mg/mL (900 and 500 rpm/s for 45 s) using the solvent chlorobenzene at 65 °C and allowed to dry for ∼12 h. An average BHJ layer thickness of 95 ± 10 nm was achieved. Electrodes made of 7 nm of Ca and 100 nm of Al were thermally evaporated onto the BHJ layer.

Decohesion Kinetics. OSCs were further processed into 1.4 × 4.0 × 50 mm testing beams as detailed elsewhere.[7] These beams were further processed into single-cantilever beam (SCB) testing specimens by fixing the beams to the rigid stage of our thin-film testing system (Delaminator DTS, Menlo Park, CA, configured for SCB testing). The SCB stage is a solid aluminum substrate with an embedded resistance heater and thermocouple. An initial crack of 3 mm was machined into the SCB specimen and subsequently loaded under tension until a crack naturally propagated into the device layers.[14] A schematic of an SCB specimen and testing procedure is summarized in Figure S10, Supporting Information. The SCB specimens were loaded to achieve an initial crack length of 10 mm, as determined by visual inspection before testing. The SCB is then covered via an aluminum block cover and sealed via an O-ring to isolate it from the atmosphere. The internal environment of the enclosure could be controlled via mass flow controllers that feed into the aluminum substrate. Nitrogen (99.9998% by volume) was fed into the chamber at a flow rate of 0.6 L min^{-1} (slight positive pressure). The nitrogen was allowed to flow into the chamber for ∼12 h prior to testing in order to minimize the amount of trace oxygen and water. The testing temperature was then changed as desired and allowed to equilibrate with the test environment. To calculate G, the SCB expression was used:[13]

$$G = \frac{6P^2a^2}{B^2E'h^3} \quad (1)$$

where P is the applied load, a is the crack length, B is the SCB specimen width, E' is the plain-strain modulus, and h is the specimen half-height. The crack length can be calculated via the beam compliance and is further discussed elsewhere. To determine decohesion growth rate, da/dt, we utilize the load relaxation technique and compliance methods to calculate crack length, a, at a given time which are related by the applied load and beam compliance. The SCB specimens were loaded to a predetermined load before the displacement was fixed. As the crack grew, the load would then relax as the crack extended through the SCB specimen. Then, da/dt was calculated using:

$$\frac{da}{dt} = -\frac{a_i P_i^{1/3}}{P^{4/3}}\frac{dP}{dt} \quad (2)$$

where a_i and P_i are the initial crack length and load at the start of the test, respectively. Experiments took place under N_2, with test

temperatures ranging from 25 to 100 °C. Tests were allowed to run for as long as 3 days, to give da/dt rates between 10^{-3} to 10^{-10} m s^{-1}.

Surface Analysis. The BHJ layer thickness was measured using a profilometer (Dektak 150+ Surface Profiler, Veeco). A scratch was induced which gave a combined thickness including the PEDOT:PSS layer and BHJ layer. The thickness of the PEDOT:PSS layer was subtracted from this. X-ray photoelectron spectroscopy (XPS) and depth profiling (PHI VersaProbe XPS Microprobe) were performed on the fracture surfaces to determine the elemental composition and to determine layer thickness. An X-ray beam spot of 200 × 200 μm with detection angle of 35 ° was used. Depth profiling was performed using Ar^+ + C_{60}^+ alternate sputtering. Ar^+ and C_{60}^+ beam currents and voltage were 3mA at 5 kV and 20 nA at 10 kV, respectively. The beams were allowed to raster over an area of 2 × 2 mm. Elemental compositions were then analyzed from the resultant spectra. Carbon K-edge near edge X-ray absorption fine structure (NEXAFS) spectroscopy was measured on the bending magnet beam line 8-2 at Stanford Synchrotron Radiation Laboratory (SSRL) (Figure S3, Supporting Information). Noncontact atomic force microscopy (AFM) (XE-70, Park Systems) was used to characterize the fracture surface topography and to obtain root-mean-squared roughness (R_q).

RESULTS AND DISCUSSION

Thermal Properties and T_g. From analysis of the total heat flow (HF) (Figure 2a) for the first heating for blends of P3HT:$PC_{60}BM$ (1:1 mass ratio), a T_g of 44.6 ± 1.7 °C for all blends (all values summarized in Table S1, Supporting Information) and a melting temperature (T_M) of 210.5 ± 2.0 °C for the P3HT phase were determined and were consistent with published DSC data for P3HT:$PC_{60}BM$ blends (M_W = 35 kDa).[15] This is important, as the Fox−Flory equation predicts that the T_g of a polymer reaches an asymptotic limit once past a critical M_W.[16] A steep shoulder prior to the melting point of the P3HT phase, which is associated with the melt crystallization of $PC_{60}BM$ is observed along with a broad melting peak at 250−270 °C, which correlates to the double melting peaks of $PC_{60}BM$ (T_g = 139.1 °C, T_M = 250.0 and 283.1 °C Figure S1, Supporting Information).[15,17]

During the second heating cycle, the reversing heat capacity (C_p^{rev}) was measured to determine whether the T_g would be affected (Figure 2b). By looking at the change in C_p^{rev} with respect to temperature, the T_g (40.5 ± 0.3 °C) becomes clearly visible as a peak (Figure 2c). This reveals that the T_g for all blends remains constant.[15] This consistency may be related to the similar P3HT dispersities (~2), thermal histories and regioregularity (~90%) (Table S2, Supporting Information) as the literature shows T_g for 1:1 blends going as high as 60 °C.[15,18,19] To understand the differences in T_g measured, we note that the literature suggests that no significant amount of phase separation between the P3HT and $PC_{60}BM$ occurs in the molten state.[15] This small change in T_g is most likely due to the different heating rates employed, and therefore we estimate T_g to be at an intermediate value.

Decohesion Kinetics. The decohesion rate measured in the BHJ layers of the OSCs are plotted as a function of G in Figure 3. Tests were performed under a nitrogen atmosphere, in order to observe the effects of P3HT M_W and test temperature without the effects of oxygen and relative humidity. Two distinct types of decohesion curves are apparent: linear and sigmoidal. The linear curves appear when decohesion occurs at $T < T_g$ of the BHJ (~45 °C) and the sigmoidal curves occur when $T > T_g$. The steep, linear curves are similar to failure in brittle materials like glasses and silicon in the absence of reactive environmental species and appreciable crack tip plasticity.[20,21] The sigmoidal curves are

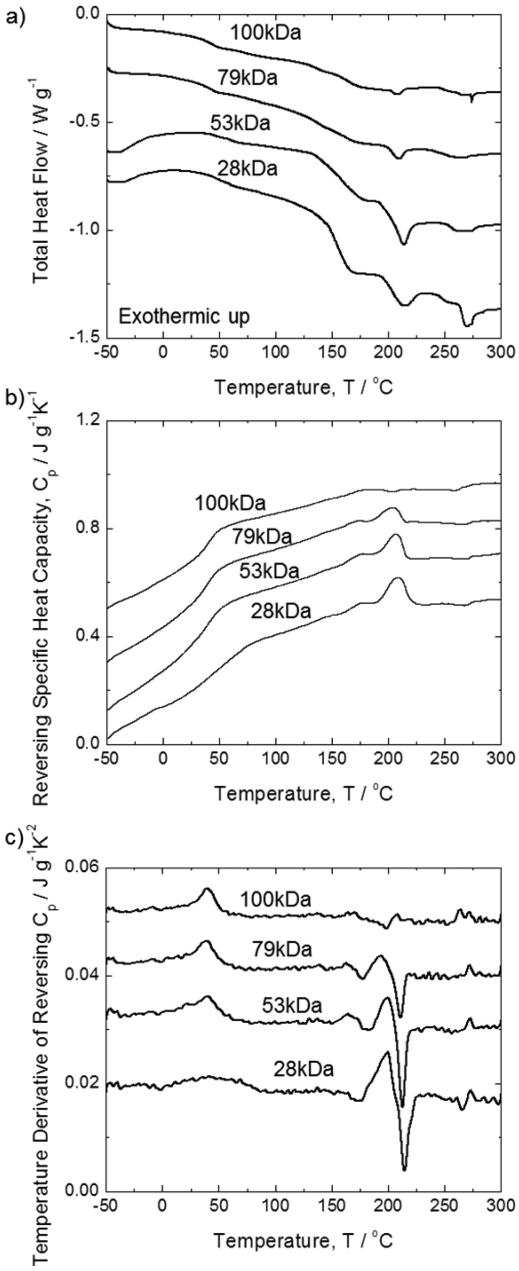

Figure 2. DSC thermogram for the (a) total HF of blends of different M_W P3HT with $PC_{60}BM$ (1:1 mass ratio). (b) MTDSC thermogram showing the C_p^{rev} and (c) dC_p^{rev}/dT. Curves were separated vertically for clarity.

characterized by three regions, as sometimes observed for failure in bulk polymers and polymer/inorganic interfaces which exhibit a time-dependent decohesion mechanism.[21−24] At low growth rates (region I, Figure 3a), a threshold region appears where decohesion rates decrease to values below ~10^{-9} m s^{-1} and where G_{th} is observed. At intermediate growth rates (region II, 10^{-8}−10^{-6} m s^{-1}), a change in the slope occurs, which is indicative of significant viscoelasticity. The slope of this region is dependent on testing temperature. At fast growth rates (region III, > 10^{-6} m s^{-1}), a steep rise in decohesion rate with G is observed and is similar to brittle fracture. This may be due to the fact that at high decohesion rates, there is little time for molecular relaxations.

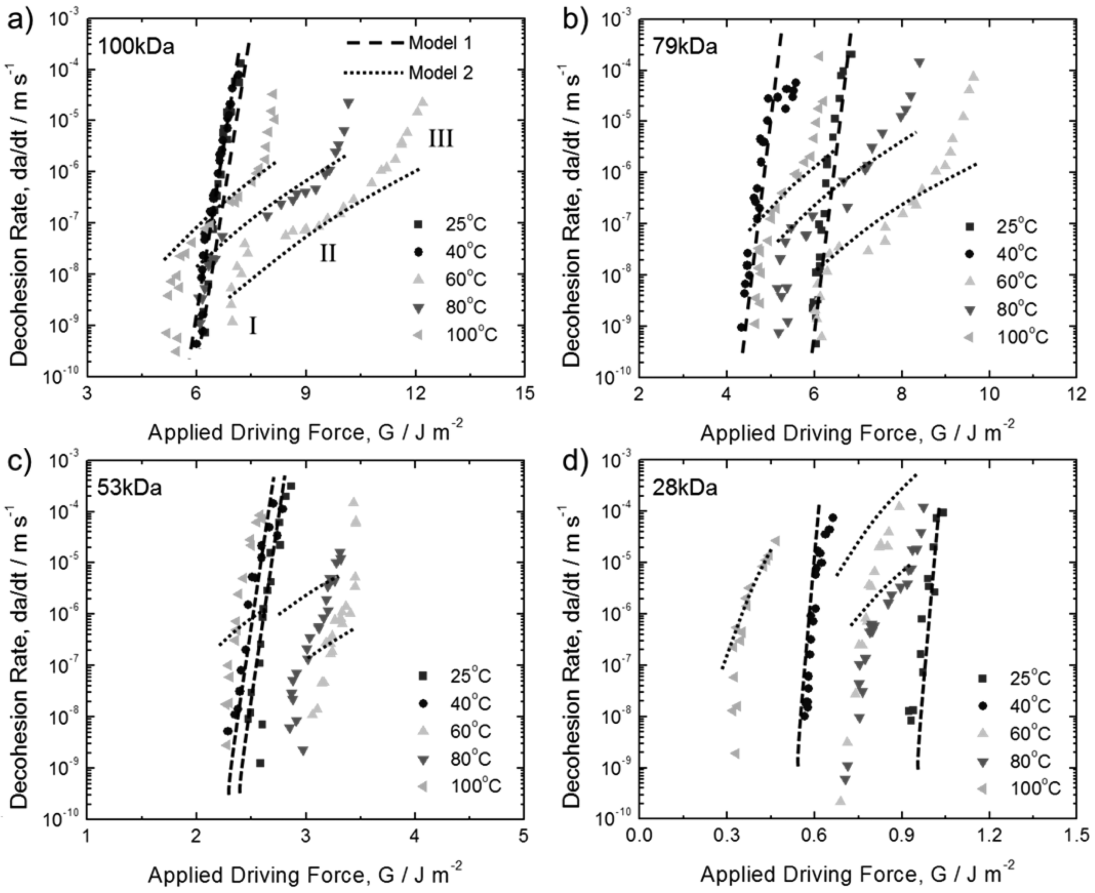

Figure 3. Decohesion growth rate curves (da/dt) as a function of applied mechanical driving force for OSC BHJ layers as a function of ambient temperature and P3HT M_W: (a) 100 kDa, (b) 79 kDa, (c) 53 kDa, and (d) 28 kDa. All tests were performed in nitrogen to eliminate the effects of oxygen and relative humidity on the decohesion rate. Decohesion curves typically deviated from a steep slope when test temperatures were above the BHJ layer T_g.

Experimental values for G_C for these blends are 10.0, 5.0, 3.5 and 1.5 J m^{-2}, for BHJs made with 100, 79, 53, and 28 kDa P3HT, respectively, indicating time-dependent decohesion well below G_C.[11] The G_{th} is plotted against testing temperature in Figure 4, and is apparent that the BHJ layer possesses a greater resistance to mechanical failure as P3HT M_W increases. Reasons for this marked increase in cohesive energy with increasing polymer M_W include a greater degree of polymer chain entanglement and greater degree of tie molecules between P3HT lamellae.[25−30] As the test temperature was raised to 40 °C, G_{th} decreases and the decohesion curves shift left, showing that increasing the test temperature lowers the applied G needed for a given decohesion rate. This may be due to an increase in polymer motion, allowing chains to more easily slide past each other. However, the effect is less pronounced for devices made with 100 and 53 kDa P3HT. This may be due to an elevation of the BHJ layer T_g due to constraint of the top and bottom glass substrates.[31] Once past the T_g, G_{th} increases and these curves shift to the right, meaning a greater G is required for a given growth rate. As testing temperatures are increased, G_{th} decreases and these curves once again shift to the left.

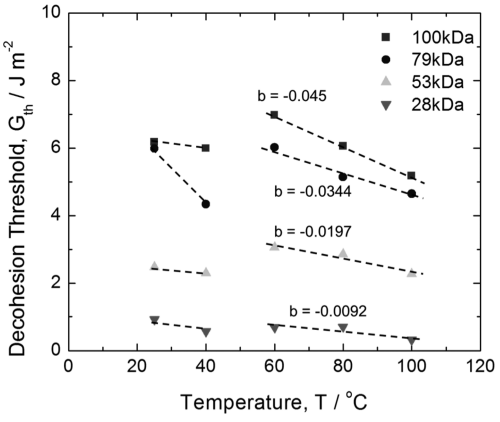

Figure 4. Threshold driving force, G_{th}, for OSC BHJs with indicated P3HT M_W is plotted against test temperatures with slope fittings when $T > T_g$. The G_{th} was taken at decohesion rates that were between 10^{-9} and 10^{-10} m s^{-1}.

The change in decohesion behavior above the T_g may be indicative of a viscoelastic decohesion growth process.[13,23,32,33] The sigmoidal shape of these curves is more pronounced at high P3HT M_W and decreases with decreasing M_W. Viscoelasticity at the decohesion tip would allow for significant plastic deformation, which helps to dissipate mechanical energy and to resist decohesion growth. This is consistent with the behavior of bulk polymers. Indeed, decohesion growth of 100 kDa P3HT without $PC_{60}BM$ is sigmoidal in shape at 25 °C in nitrogen (T_g ~12.1 °C for pure P3HT, Figures S1 and S2, Supporting Information), which suggests that viscoelasticity within the polymer phase is responsible for this behavior. The

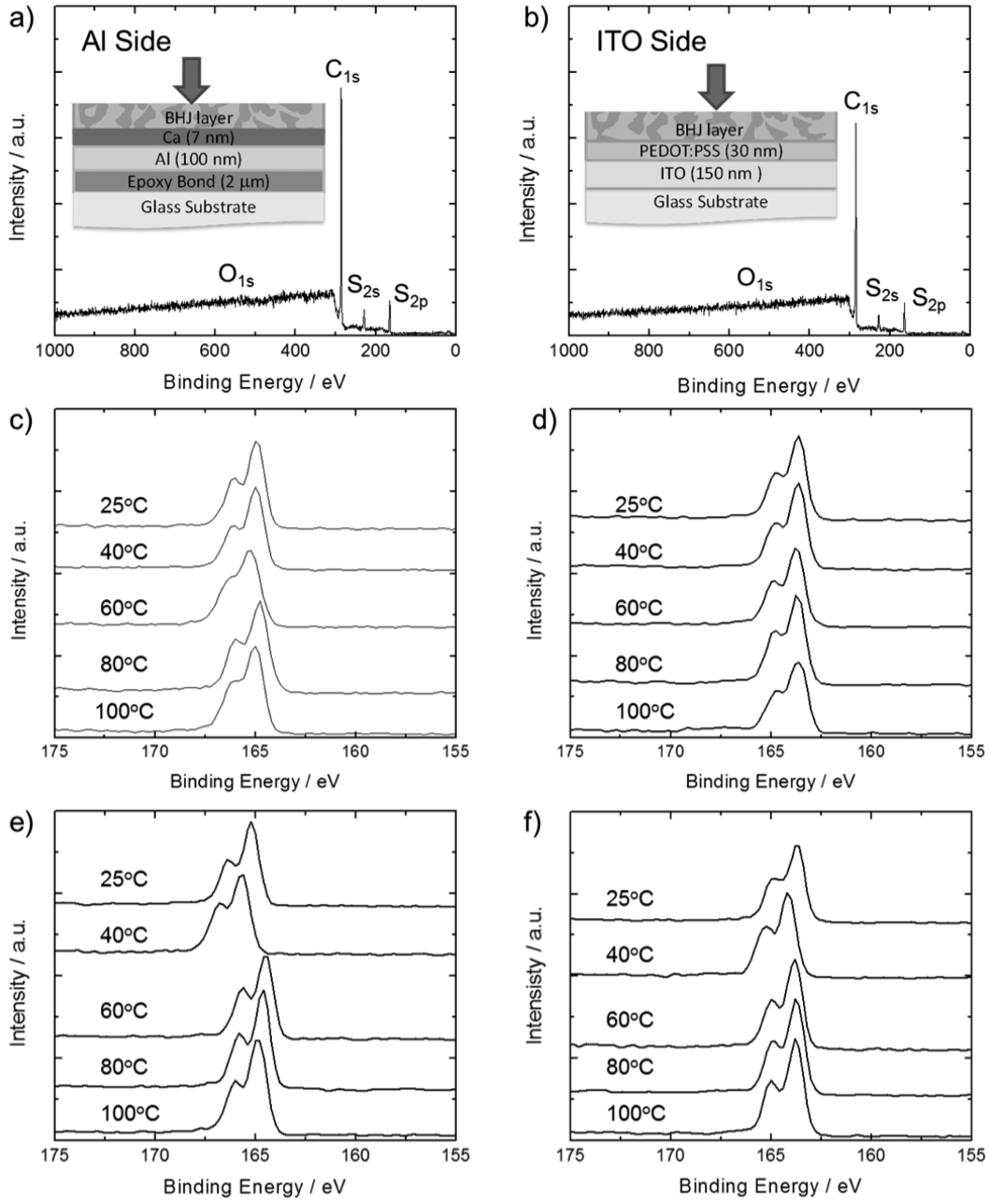

Figure 5. XPS spectra of fractured surfaces for OSC made using 100 kDa P3HT (25 °C, in N_2) from the (a) Al side (left column) and the (b) ITO side (right column). High resolution spectra of the S_{2p} peak for surfaces of OSCs made from 100 kDa P3HT (c and d) and 28 kDa P3HT (e and f).

increase of the slope of the intermediate region (II) with increasing temperature indicates greater sensitivity to G. This is consistent with viscoelasticity and a reduction in the relaxation modulus.[13] Studies have shown that a plateau in the da/dt vs G curve is due to limited diffusion of chemically active species to the strained chemical bonds at the decohesion tip.[14,22] However, because our testing system is under nitrogen, chemical reactivity is unlikely to explain decohesion growth in this region.

Surface Analysis. To determine the crack growth path within the organic solar cell, high-resolution X-ray photoelectron spectroscopy (XPS) was employed for all devices to determine the precise elemental and chemical composition of the fractured surfaces. Near-edge X-ray absorption fine structure (NEXAFS) spectroscopy was performed on critically failed devices at room temperature in air to show that cohesive and not adhesive failure was the primary failure mode (Figures S3 and S4, Supporting Information). Therefore, high resolution XPS of the S_{2p} core level (155−175 eV) was determined to be sufficiently sensitive enough to differentiate between P3HT and PEDOT:PSS should interfacial debonding occur. From Figure 5a,b, we see typical XPS spectra of the top and bottom cohesive surfaces with matching in elemental composition (~90% C, 8% S, and 2% O) indicative of cohesive failure. High resolution images of the S_{2p} peak for matching cohesive surfaces of the BHJ layers are also shown for 100 kDa P3HT (Figure 5c,d) and 28 kDa (Figure 5e,f) (53 kDa and 79 kDa in Figure S7, Supporting Information). Each show unambiguously, a single sulfur signal ($2p_{1/2}$ and $2p_{3/2}$ doublet) at about 165 eV, which may be attributed to P3HT, indicating cohesive failure within the BHJ layer for all these devices at all temperatures.

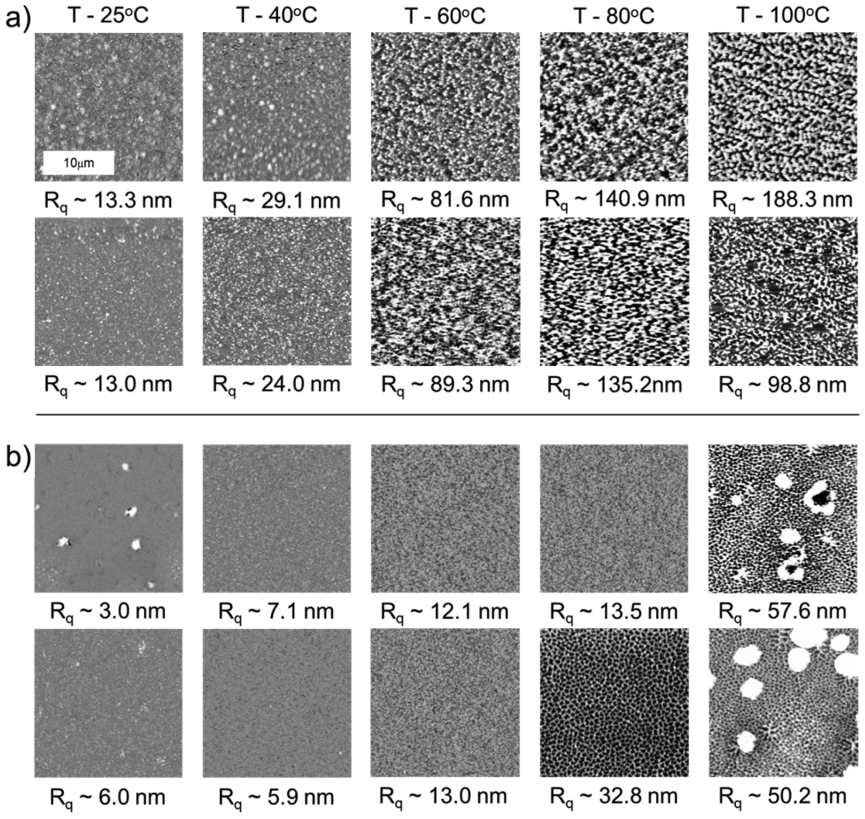

Figure 6. AFM topographic images for conjugate fracture surfaces (top row = Al side, bottom row = ITO side) of OSCs made with (a) 100 kDa and (b) 28 kDa P3HT debonded at the indicated test temperature.

PEDOT:PSS typically displays two S_{2p} peaks, one at 165 eV and one at 170 eV, for both the PEDOT and PSS species, respectively (reference spectra Figure S5, Supporting Information). The peak at 170 eV appears because PSS is the only chemical species with a sulfonate group (S═O).[34] Therefore, we can say that the change decohesion kinetics when going from 40 to 60 °C is not due to interfacial failure between the P3HT:$PC_{60}BM$ and PEDOT:PSS. Indeed, AFM images for the matching decohesion surfaces indicate similar root-mean-square roughness values (Figure 6). The increase in surface roughness with test temperature would also indicate significant amounts of plastic yielding occurs at the crack tip as chains are pulled in tension and aligned. To determine whether the failure path would change where cohesive failure would occur within the BHJ layer, depth profiling on the cohesive surface that contained ITO was performed (Figure 7).[35] From this, we see that with increasing temperatures, the crack tends to move closer to the center of the BHJ layer, which is consistent with the literature, indicating the decohesion position would move toward the center of the BHJ layer with thermal annealing.[7] This may be due to the fact that $PC_{60}BM$ tends to phase separate toward the top contact (Ca/Al), away from the PEDOT:PSS layer, during thermal annealing.[36−38] Indeed, during thermal annealing, studies have shown a greater degree of miscibility between the P3HT and $PC_{60}BM$ phase and the vertical diffusion of $PC_{60}BM$ greatly alters device morphology and characteristics.[39−41]

Modeling Decohesion Kinetics. For decohesion below T_g, we employ a decohesion kinetic model that has been used for brittle polymers, bulk glasses, and polymer/metal interfaces:[12,42,43]

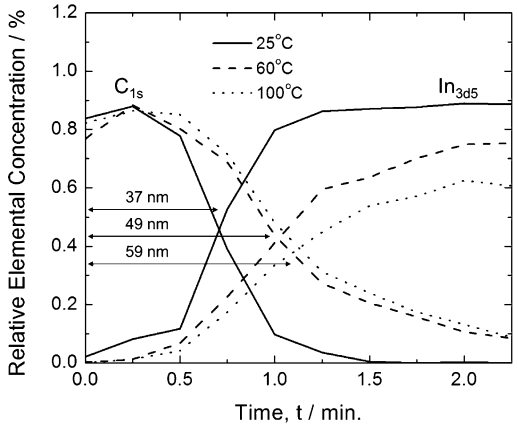

Figure 7. Relative elemental concentration for sputtered fracture surface (ITO side) of OSCs made using 100 kDa P3HT and debonded at indicated temperature.

$$\frac{da}{dt} = v_0 \sinh\left(\frac{G - 2\gamma}{\eta}\right) \tag{3}$$

where G is the applied driving force, v_0 is a proportionality constant related to the chemical structure and local environment at the decohesion tip, 2γ is the surface energy, and η is equal to

$$\eta = 2Nk_BT \tag{4}$$

where N is the effective bond area density, k_B is the Boltzmann constant, and T is the testing temperature. The models were then fitted to the data in Figure 3. It was observed that 2γ

dx.doi.org/10.1021/am506482q | ACS Appl. Mater. Interfaces 2014, 6, 21474−21483

shifted to lower values when T was increased from 25 to 40 °C, indicating a reduction in the applied G needed for decohesion.

For test temperatures above T_g, the model does not account for the inherent viscoelastic processes that give rise to the pronounced sigmoidal shape of the curves. Instead, we extended a polymer fracture kinetics model that we recently modified for EVA/glass interfaces where viscoelastic effects at the decohesion tip are significant.[13] Our new model explicitly includes the effects of temperature and polymer M_W and captures the intermediate growth rate region (II). The central assumption is that the decohesion rate, da/dt, can be modeled by the rate of formation of a viscoelastic zone of size r_p ahead of the decohesion tip:

$$\frac{da}{dt} = \frac{r_p}{\tau} \tag{5}$$

where τ is the relaxation time of the polymer, which represents an estimate of the time needed to form the viscoelastic zone. The zone r_p can be estimated by[32,44,45]

$$r_p = \frac{\pi}{8}\frac{\delta_c}{\varepsilon_y} \tag{6}$$

where δ_c is the critical crack tip opening displacement and ε_y is the yield strain of the material. Viscoelastic decohesion in polymers occurs when[32,44]

$$G = \delta_c \varepsilon_y E \tag{7}$$

where E is the relaxation modulus. The viscoelastic decohesion process depends on test temperature and polymer M_W and we explicitly include this dependency in the model as follows. The time dependence of E can be described with a power-law equation, based on viscoelastic relaxation mechanics:[32,44,45]

$$E = E_1 \tau_{T_0}^{-n} \tag{8}$$

where τ_{T_0} is the elapsed relaxation time at a reference temperature, T_0, E_1 is the modulus at unit time, and n is a measure of the rate sensitivity of the material ($n = 0$ for perfectly elastic solids). Using eqs 7 and 8, and solving for τ_{T_0}

$$\tau_{T_0} = \left(\frac{E}{E_1}\right)^{-1/n} = \left(\frac{G}{\delta_c \varepsilon_y E_1}\right)^{-1/n} \tag{9}$$

We then use the Williams–Landel–Ferry (WLF) time–temperature superposition principle to estimate the effect of temperature, T, on the relaxation time as follows[46]

$$\tau = \tau_{T_0} a_T \tag{10}$$

where a_T is the WLF time–temperature "shift" factor as described by

$$a_T = 10^{-C_a(T-T_g)/C_b+(T-T_g)} \tag{11}$$

where C_a=17.1, C_b = 51.6 K^{-1}. The polymer M_W influences the relaxation time according to[47]

$$\tau = \tau_{M_0} e^{-B\left(\frac{1}{M_w}-\frac{1}{M_0}\right)} \tag{12}$$

where τ_{M_0} is the relaxation time at T_0 and reference molecular weight, M_0. The term B is an empirical constant for the polymer that we assume is independent of temperature. Finally, using eqs 9, 10, and 12, the relaxation time as a function of G, T, and M_W is given by

$$\tau = \left(\frac{G}{\delta_c \varepsilon_y E_1}\right)^{-1/n} \cdot 10^{-C_a(T-T_0)/C_b+(T-T_0)} \cdot e^{-B\left(\frac{1}{M_w}-\frac{1}{M_0}\right)} \tag{13}$$

Substituting eq 13 into eq 5 gives

$$\frac{da}{dt} = \frac{\pi}{8}\frac{\delta_c}{\varepsilon_y(\delta_c \varepsilon_y E_1)^{1/n}}(G)^{1/n} \cdot 10^{C_a(T-T_g)/C_b+(T-T_g)} \cdot e^{B\left(\frac{1}{M_w}-\frac{1}{M_0}\right)} \tag{14}$$

Equation 14 was applied to the data in Figure 3 and accurately describes decohesion in the intermediate region (II) for BHJs using 53 kDa P3HT or higher. From the fitting, we were able to calculate reasonable values for $B = 6 \times 10^5$ Da and $M_0 = 4 \times 10^4$ Da. Temperature and M_W-dependent δ_c values were estimated using the feature sizes of the BHJ cohesive surfaces from AFM scans (Figures 6, S8, and S9, Supporting Information). The values given for ε_y, which were less sensitive to temperature and M_W, were in the range of 0.04 to 0.06, which is typical for noncross-linked polymers such as polyethylene and poly(vinyl chloride).[48] Values are given in Table 1 (all other constants are given in Table S3, Supporting Information which includes values from other studies).[49] This modeling would indicate that temperature sensitive viscoelastic processes drive decohesion in the intermediate growth regime.

Table 1. Table of Fitting Parameters for Decohesion Growth Models above and below T_g[a]

parameters				
M_W (Da)	T (°C)	N (bonds m^{-2})	δ_c (nm)[b]	ε_y
100000	60	1.1×10^{19}	190	0.06
	80		310	
	100		410	
79000	60	8×10^{18}	180	0.06
	80		260	
	100		340	
53000	60	4×10^{18}	110	0.05
	80		180	
	100		280	
28000	60	1.2×10^{18}	60	0.04
	80		100	
	100		120	

[a]Values for δ_c were estimated from surface feature sizes from AFM scans. [b]Estimated using surface feature size from AFM

However, at high growth rates (10^{-6} m s^{-1} < da/dt), we observe a sharp increase da/dt with G, which is similar to brittle fracture. This may indicate that at high rates, there is not enough time for viscoelastic relaxation processes to significantly affect decohesion. Additionally, the model over predicts low growth rates (<10^{-9} m s^{-1}) where a threshold in the experimental data is expected.[11] It has been suggested that at low growth rates with decreasing G, $\delta < \delta_c$ and at these conditions, decohesion will arrest.[23] Additionally, the model does not capture the decohesion behavior as well for the low molecular weight P3HT BHJs. This may be due to the fact that at such low M_W, fewer entanglements between polymer chains are likely, reducing the viscoelasticity of the BHJ layer significantly.

To understand the mechanism behind viscoelastic decohesion, we note that experiments have shown that debonding occurs readily with increasing $PC_{60}BM$ content, indicating weaker regions where $PC_{60}BM$ aggregates.[7,50] Additionally, for

semicrystalline polymers, decohesion is often characterized by the amorphous and crystalline regions being drawn and aligned along the strain axis, leaving voids.[51,52] Therefore, it is likely that viscoelastic decohesion initiates via the growth of voids in front of the decohesion tip. This allows for the growth of polymer crazes characteristic of plastic deformation.[48] Overtime, the polymer chains within the crazes slide past each other, extending decohesion. At some point, the voids are able to coalesce and a crack surface is produced.

It is interesting to note that although the MTDSC data points to a T_g of 40.5 °C, viscoelastic decohesion is not observed at test temperatures of 40 °C, which may indicate that T_g is higher than 40.5 °C. This may also have to do with the fact that the relative $PC_{60}BM$ concentration will shift the observed T_g, meaning some solar cells may have had relatively higher $PC_{60}BM$ concentrations near the decohesion tip. Indeed, studies have shown that $PC_{60}BM$ readily diffuses through the polymer matrix even under confinement at temperatures used for annealing.[17,53] More interesting is the fact that while the adjacent PEDOT:PSS layer is relatively thin (∼30 nm), failure does not occur there for the temperature range of interest. Although PEDOT:PSS does not possess a clear T_g, it does have a T_M of ∼300 °C and a degradation temperature of ∼230 °C.[54] Studies have indicated that at higher temperatures, an electrochemical reaction occurs between P3HT and PSS, forming $P3HT^+$ and PSS^-.[55] These studies suggest that stronger interfacial bonding occurs that prevents decohesion from occurring within the PEDOT:PSS layer.

CONCLUSION

In conclusion, we have characterized and modeled the decohesion kinetics of OSC BHJ layers consisting of P3HT (varying M_W) and hole conductor $PC_{60}BM$. We determined that within a nitrogen environment, molecular decohesion within the BHJ readily occurs at driving forces below G_C. However, the decohesion curves become sigmoidal in shape when test temperatures were raised to 60 °C. From thermal analysis, it was revealed that the BHJ layer possessed a T_g of ∼41−45 °C, regardless of P3HT M_W. Surface topography revealed a dramatic increase in surface roughness for cohesive surfaces tested above T_g, revealing significant plastic deformation.

We therefore attribute the significant plastic deformation at high T to the BHJ layer undergoing a transition into the rubbery state leading to significant viscoelasticity. At these high temperatures, we observed that decohesion growth was driven via viscoelastic relaxation processes. Additionally, we observed that G_{th} decreases with increasing T, reducing the barrier to film decohesion. From this, we derived a viscoelastic decohesion model that accounts for the effect of temperature and P3HT M_W. Future studies should incorporate the effects of oxygen, moisture, and UV light to determine if there are synergistic effects that could reduce device reliability. By leveraging these insights, we come closer to designing mechanically robust BHJ OSCs and other organic electronics that utilize polymer thin films.

ASSOCIATED CONTENT

Supporting Information

Polymer batch information, BHJ layer spin coating parameters, solar cell performance, optical/AFM image for debond surface of 28 kDa P3HT based organic, compliance vs debond length for four point bend test, and four point bend schematic. This material is available free of charge via the Internet at http://pubs.acs.org.

AUTHOR INFORMATION

Corresponding Author

*Reinhold Dauskardt. Address: Department of Materials Science and Engineering, 496 Lomita Mall, Durand Building, Stanford, CA 94305-2205. E-mail: dauskardt@stanford.edu.

Author Contributions

The paper was written through contributions of all authors. All authors have given approval to the final version of the paper.

Funding

This work was supported by the Center for Advanced Molecular Photovoltaics (CAMP) under the King Abdullah University of Science and Technology (KAUST) under award no. KUS-C1-015-21.

Notes

The authors declare no competing financial interest.

REFERENCES

(1) Krebs, F. C. Fabrication and Processing of Polymer Solar Cells: A Review of Printing and Coating Techniques. *Sol. Energy Mater. Sol. Cells* **2009**, *93*, 394−412.

(2) Scharber, M. C.; Sariciftci, N. S. Efficiency of Bulk-Heterojunction Organic Solar Cells. *Prog. Polym. Sci.* **2013**, *38*, 1929−1940.

(3) Cantatore, E. *Applications of Organic and Printed Electronics*. Springer: New York, 2012.

(4) Lipomi, D. J.; Chong, H.; Vosgueritchian, M.; Mei, J. G.; Bao, Z. A. Toward Mechanically Robust and Intrinsically Stretchable Organic Solar Cells: Evolution of Photovoltaic Properties with Tensile Strain. *Sol. Energy Mater. Sol. Cells* **2012**, *107*, 355−365.

(5) Krebs, F. C.; Espinosa, N.; Hosel, M.; Sondergaard, R. R.; Jorgensen, M. 25th Anniversary Article: Rise to Power - OPV-based Solar Parks. *Adv. Mater.* **2014**, *26*, 29−39.

(6) Grossiord, N.; Kroon, J. M.; Andriessen, R.; Blom, P. W. M. Degradation Mechanisms in Organic Photovoltaic Devices. *Org. Electron.* **2012**, *13*, 432−456.

(7) Brand, V.; Bruner, C.; Dauskardt, R. H. Cohesion and Device Reliability in Organic Bulk Heterojunction Photovoltaics. *Sol. Energy Mater. Sol. Cells* **2012**, *99*, 182−189.

(8) Dupont, S. R.; Oliver, M.; Krebs, F. C.; Dauskardt, R. H. Interlayer Adhesion in Roll-to-Roll Processed Flexible Inverted Polymer Solar Cells. *Sol. Energy Mater. Sol. Cells* **2012**, *97*, 171−175.

(9) Brand, V.; Levi, K.; McGehee, M. D.; Dauskardt, R. H. Film Stresses and Metal Electrode Buckling in Organic Bulk Heterojunction Solar Cells. *Sol. Energy Mater. Sol. Cells* **2012**, *103*, 80−85.

(10) Bruner, C.; Miller, N. C.; McGehee, M. D.; Dauskardt, R. H. Molecular Intercalation and Cohesion of Organic Bulk Heterojunction Photovoltaic Devices. *Adv. Funct. Mater.* **2013**, *23*, 2863−2871.

(11) Bruner, C.; Dauskardt, R. H. Role of Molecular Weight on the Mechanical Device Properties of Organic Polymer Solar Cells. *Macromolecules* **2014**, *47*, 1117−1121.

(12) Dupont, S. R.; Novoa, F.; Voroshazi, E.; Dauskardt, R. H. Decohesion Kinetics of PEDOT:PSS Conducting Polymer Films. *Adv. Funct. Mater.* **2014**, *24*, 1325−1332.

(13) Novoa, F. D.; Miller, D. C.; Dauskardt, R. H. Environmental mechanisms of debonding in photovoltaic backsheets. *Sol. Energy Mater. Sol. Cells* **2014**, *120*, 87−93.

(14) Birringer, R. P.; Shaviv, R.; Besser, P. R.; Dauskardt, R. H. Environmentally Assisted Debonding of Copper/Barrier Interfaces. *Acta Mater.* **2012**, *60*, 2219−2228.

(15) Zhao, J.; Swinnen, A.; Van Assche, G.; Manca, J.; Vanderzande, D.; Van Mele, B. Phase Diagram of P3HT/PCBM Blends and Its Implication for the Stability of Morphology. *J. Phys. Chem. B* **2009**, *113*, 1587−1591.

(16) Fox, T. G.; Loshaek, S. Influence of Molecular Weight and Degree of Crosslinking on the Specific Volume and Glass Temperature of Polymers. *J. Polym. Sci.* **1955**, *15*, 371−390.
(17) Watts, B.; Belcher, W. J.; Thomsen, L.; Ade, H.; Dastoor, P. C. A Quantitative Study of PCBM Diffusion during Annealing of P3HT:PCBM Blend Films. *Macromolecules* **2009**, *42*, 8392−8397.
(18) Hopkinson, P. E.; Staniec, P. A.; Pearson, A. J.; Dunbar, A. D. F.; Wang, T.; Ryan, A. J.; Jones, R. A. L.; Lidzey, D. G.; Donald, A. M. A Phase Diagram of the P3HT:PCBM Organic Photovoltaic System: Implications for Device Processing and Performance. *Macromolecules* **2011**, *44*, 2908−2917.
(19) Muller, C.; Ferenczi, T. A. M.; Campoy-Quiles, M.; Frost, J. M.; Bradley, D. D. C.; Smith, P.; Stingelin-Stutzmann, N.; Nelson, J. Binary Organic Photovoltaic Blends: A Simple Rationale for Optimum Compositions. *Adv. Mater.* **2008**, *20*, 3510−3515.
(20) Fitzgerald, A. M.; Iyer, R. S.; Dauskardt, R. H.; Kenny, T. W. Subcritical Crack Growth in Single-crystal Silicon using Micromachined Specimens. *J. Mater. Res.* **2002**, *17*, 683−692.
(21) Wiederhorn, S. M.; Fuller, E. R.; Thomson, R. Micromechanisms of Crack-Growth in Ceramics and Glasses in Corrosive Environments. *Met. Sci.* **1980**, *14*, 450−458.
(22) Kook, S. Y.; Dauskardt, R. H. Moisture-Assisted Subcritical Debonding of a Polymer/Metal Interface. *J. Appl. Phys.* **2002**, *91*, 1293−1303.
(23) Williams, J. G.; Marshall, G. P. Environmental Crack and Craze Growth Phenomena in Polymers. *Proc. R. Soc. London, Ser. A* **1975**, *342*, 55−77.
(24) Kook, S. Y.; Snodgrass, J. M.; Kirtikar, A.; Dauskardt, R. H. Adhesion and Reliability of Polymer/Inorganic Interfaces. *J. Electron. Packag.* **1998**, *120*, 328−335.
(25) Zhao, K.; Khan, H. U.; Li, R. P.; Su, Y. S.; Amassian, A. Entanglement of Conjugated Polymer Chains Influences Molecular Self-Assembly and Carrier Transport. *Adv. Funct. Mater.* **2013**, *23*, 6024−6035.
(26) Brinkmann, M.; Rannou, P. Effect of Molecular Weight on the Structure and Morphology of Oriented Thin Films of Regioregular Poly(3-hexylthiophene) Grown by Directional Epitaxial Solidification. *Adv. Funct. Mater.* **2007**, *17*, 101−108.
(27) Brinkmann, M.; Rannou, P. Molecular Weight Dependence of Chain Packing and Semicrystalline Structure in Oriented Films of Regioregular Poly(3-hexylthiophene) Revealed by High-Resolution Transmission Electron Microscopy. *Macromolecules* **2009**, *42*, 1125−1130.
(28) Kline, R. J.; McGehee, M. D.; Kadnikova, E. N.; Liu, J. S.; Frechet, J. M. J. Controlling the Field-Effect Mobility of Regioregular Polythiophene by Changing the Molecular Weight. *Adv. Mater.* **2003**, *15*, 1519−1522.
(29) Koppe, M.; Brabec, C. J.; Heiml, S.; Schausberger, A.; Duffy, W.; Heeney, M.; McCulloch, I. Influence of Molecular Weight Distribution on the Gelation of P3HT and Its Impact on the Photovoltaic Performance. *Macromolecules* **2009**, *42*, 4661−4666.
(30) Koch, F. P. V.; Rivnay, J.; Foster, S.; Muller, C.; Downing, J. M.; Buchaca-Domingo, E.; Westacott, P.; Yu, L. Y.; Yuan, M. J.; Baklar, M.; Fei, Z. P.; Luscombe, C.; McLachlan, M. A.; Heeney, M.; Rumbles, G.; Silva, C.; Salleo, A.; Nelson, J.; Smith, P.; Stingelin, N. The Impact of Molecular Weight on Microstructure and Charge Transport in Semicrystalline Polymer Semiconductors Poly(3-hexylthiophene), a Model Study. *Prog. Polym. Sci.* **2013**, *38*, 1978−1989.
(31) Aharoni, S. M. Increased Glass Transition Temperature in Motionally Constrained Semicrystalline Polymers. *Polym. Adv. Technol.* **1998**, *9*, 169−201.
(32) Bradley, W.; Cantwell, W. J.; Kausch, H. H. Viscoelastic Creep Crack Growth: A Review of Fracture Mechanical Analyses. *Mech. Time-Depend. Mater.* **1998**, *1*, 241−268.
(33) Andrews, E. H.; Kinloch, A. J. Mechanics of Adhesive Failure .1. *Proc. R. Soc. London, Ser. A* **1973**, *332*, 385−399.
(34) Greczynski, G.; Kugler, T.; Salaneck, W. R. Characterization of the PEDOT-PSS System by Means of X-ray and Ultraviolet Photoelectron Spectroscopy. *Thin Solid Films* **1999**, *354*, 129−135.
(35) Yu, B. Y.; Chen, Y. Y.; Wang, W. B.; Hsu, M. F.; Tsai, S. P.; Lin, W. C.; Lin, Y. C.; Jou, J. H.; Chu, C. W.; Shyue, J. J. Depth Profiling of Organic Films with X-ray Photoelectron Spectroscopy Using C(60)(+) and Ar(+) Co-sputtering. *Anal. Chem.* **2008**, *80*, 3412−3415.
(36) Parnell, A. J.; Dunbar, A. D. F.; Pearson, A. J.; Staniec, P. A.; Dennison, A. J. C.; Hamamatsu, H.; Skoda, M. W. A.; Lidzey, D. G.; Jones, R. A. L. Depletion of PCBM at the Cathode Interface in P3HT/PCBM Thin Films as Quantified via Neutron Reflectivity Measurements. *Adv. Mater.* **2010**, *22*, 2444−2447.
(37) Ruderer, M. A.; Guo, S.; Meier, R.; Chiang, H.; Körstgens, V.; Wiedersich, J.; Perlich, J.; Roth, S. V.; Müller-Buschbaum, P. Solvent-Induced Morphology in Polymer-based Systems for Organic Photovoltaics. *Adv. Funct. Mater.* **2011**, *21*, 3382−3391.
(38) Guo, S.; Ruderer, M. A.; Rawolle, M.; Körstgens, V.; Birkenstock, C.; Perlich, J.; Müller-Buschbaum, P. Evolution of Lateral Structures During the Functional Stack Build-up of P3HT:PCBM-Based Bulk Heterojunction Solar Cells. *ACS Appl. Mater. Interfaces* **2013**, *5*, 8581−8590.
(39) Xu, Z.; Chen, L. M.; Yang, G. W.; Huang, C. H.; Hou, J. H.; Wu, Y.; Li, G.; Hsu, C. S.; Yang, Y. Vertical Phase Separation in Poly(3-hexylthiophene): Fullerene Derivative Blends and Its Advantage for Inverted Structure Solar Cells. *Adv. Funct. Mater.* **2009**, *19*, 1227−1234.
(40) Treat, N. D.; Brady, M. A.; Smith, G.; Toney, M. F.; Kramer, E. J.; Hawker, C. J.; Chabinyc, M. L. Interdiffusion of PCBM and P3HT Reveals Miscibility in a Photovoltaically Active Blend. *Adv. Energy Mater.* **2011**, *1*, 145−145.
(41) Bartelt, J. A.; Beiley, Z. M.; Hoke, E. T.; Mateker, W. R.; Douglas, J. D.; Collins, B. A.; Tumbleston, J. R.; Graham, K. R.; Amassian, A.; Ade, H.; Frechet, J. M. J.; Toney, M. F.; McGehee, M. D. The Importance of Fullerene Percolation in the Mixed Regions of Polymer-Fullerene Bulk Heterojunction Solar Cells. *Adv. Energy Mater.* **2013**, *3*, 364−374.
(42) Lawn, B. R. Diffusion-Controlled Subcritical Crack Growth in Presence of a Dilute Gas Environment. *Mater. Sci. Eng.* **1974**, *13*, 277−283.
(43) Wiederhorn, S. M.; Bolz, L. H. Stress Corrosion and Static Fatigue of Glass. *J. Am. Ceram. Soc.* **1970**, *53*, 543−548.
(44) Marshall, G. P.; Coutts, L. H.; Williams, J. G. Temperature Effects in Fracture of PMMA. *J. Mater. Sci.* **1974**, *9*, 1409−1419.
(45) Schapery, R. A. Method for Predicting Crack Growth in Nonhomogeneous Viscoelastic Media. *Int. J. Fract.* **1978**, *14*, 293−309.
(46) Williams, M. L.; Landel, R. F.; Ferry, J. D. Temperature Dependence of Relaxation Mechanisms in Amorphous Polymers and Other Glass-Forming Liquids. *Phys. Rev.* **1955**, *98*, 1549−1549.
(47) Michel, J.; Manson, J. A.; Hertzberg, R. W. A Simple Viscoelastic Model for Fatigue Crack-Propagation in Polymers as a Function of Molecular-Weight. *Polymer* **1984**, *25*, 1657−1666.
(48) Sperling, L. H. *Introduction to Physical Polymer Science*, 4th ed.; Wiley: Hoboken, NJ, 2006; p 845.
(49) Savagatrup, S.; Makaram, A. S.; Burke, D. J.; Lipomi, D. J. Mechanical Properties of Conjugated Polymers and Polymer-Fullerene Composites as a Function of Molecular Structure. *Adv. Funct. Mater.* **2014**, *24*, 2264−2264.
(50) Gent, A. N. Detachment of an Elastic Matrix from a Rigid Spherical Inclusion. *J. Mater. Sci.* **1980**, *15*, 2884−2888.
(51) Kausch, H. H.; Devries, K. L. Molecular Aspects of High Polymer Fracture as Investigated by ESR-Technique. *Int. J. Fract.* **1975**, *11*, 727−759.
(52) Hornbogen, E.; Friedrich, K. On the Use of Partial Properties to Interpret the Bulk Crack-Propagation Behavior of Coarse 2-Phase Materials. *J. Mater. Sci.* **1980**, *15*, 2175−2182.
(53) Yang, X. N.; Alexeev, A.; Michels, M. A. J.; Loos, J. Effect of Spatial Confinement on the Morphology Evolution of Thin Poly(p-phenylenevinylene)/Methanofullerene Composite Films. *Macromolecules* **2005**, *38*, 4289−4295.

(54) Skotheim, T. A.; Reynolds, J. R. *Handbook of Conducting Polymers. Conjugated Polymers: Processing and Applications*, 3rd ed.; CRC Press: Boca Raton, FL, 2007.
(55) Huang, D. M.; Mauger, S. A.; Friedrich, S.; George, S. J.; Dumitriu-LaGrange, D.; Yoon, S.; Moule, A. J. The Consequences of Interface Mixing on Organic Photovoltaic Device Characteristics. *Adv. Funct. Mater.* **2011**, *21*, 1657−1665.